Supplemental Material

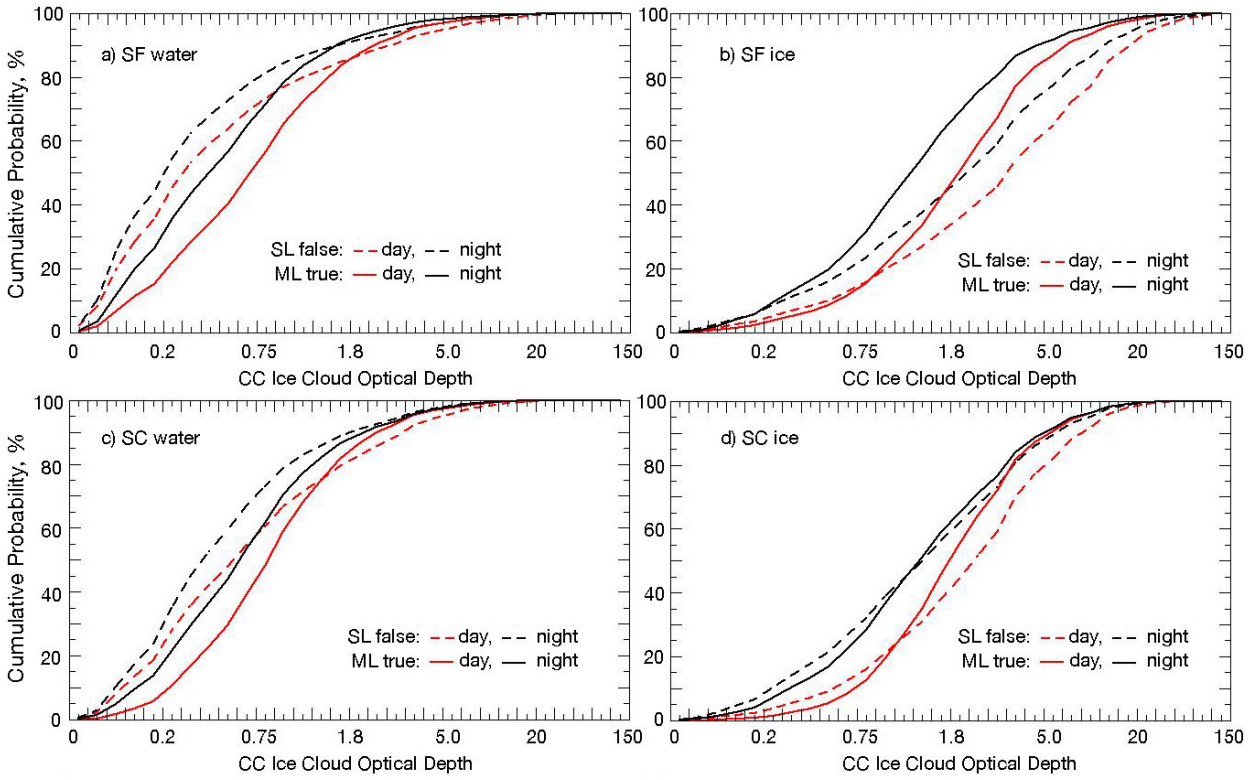

Fig. S1. Cumulative probability distributions of 2009 false SL and true ML clouds from MLANN as functions of upper-layer cloud optical depth for ice (left) and water (right) phase clouds over snow free (top) and snow/ice covered (bottom) surfaces. The major tick marks for the x-axes on the top panels are 0, 0.0025, 0.05. 0.1, 0.15, 0.2, 0.3, 0.4, 0.5, 0.6, 0.75, 0.9, 1.1, 1.3, 1.5, 1.8, 2.1, 2.5, 3, 4, 5, 6, 8, 10, 15, 20, 30, 40, 60, 80, and 150.

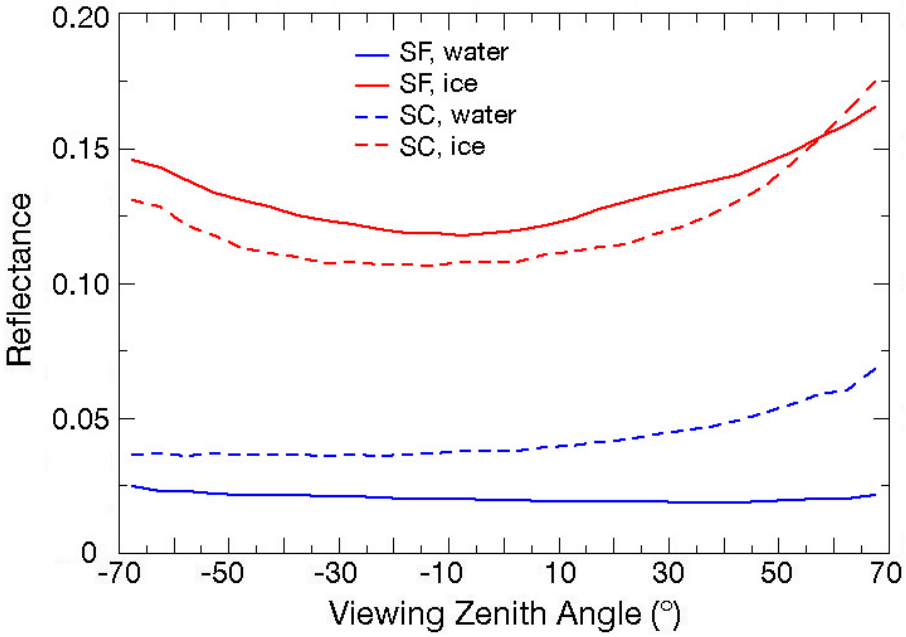

Fig. S2. Global average 1.38-µm reflectance as a function of viewing zenith angle for JAJO 2019.

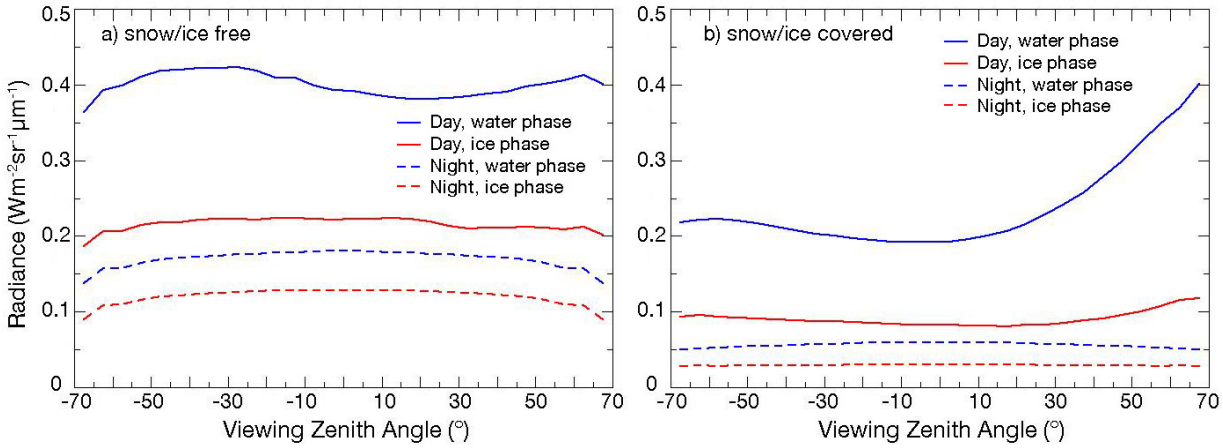

Fig. S3. Global average 3.75-μm radiance as a function of viewing zenith angle for JAJO 2019.

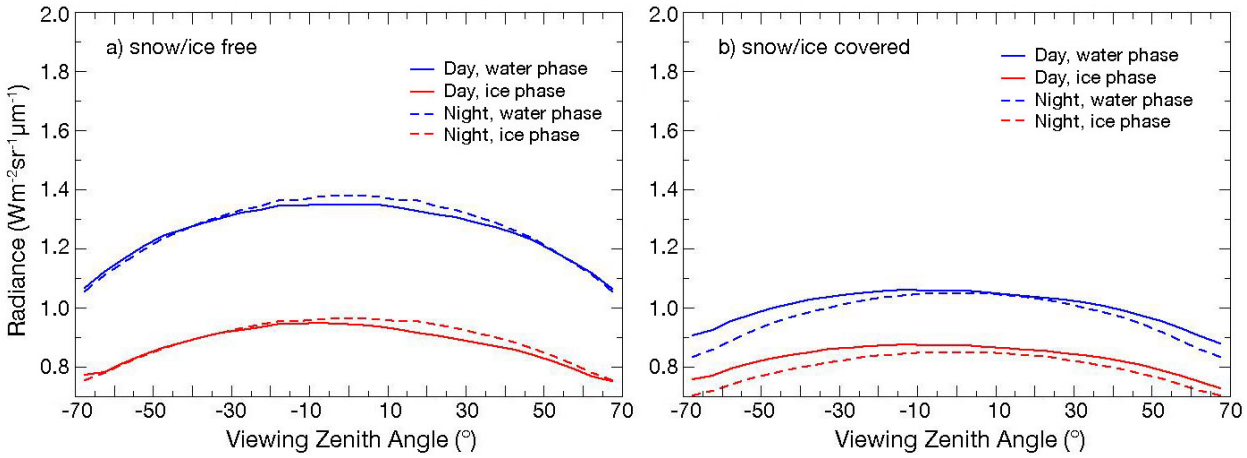

Fig. S4. Global average 6.70-μm radiance as a function of viewing zenith angle for JAJO 2019.

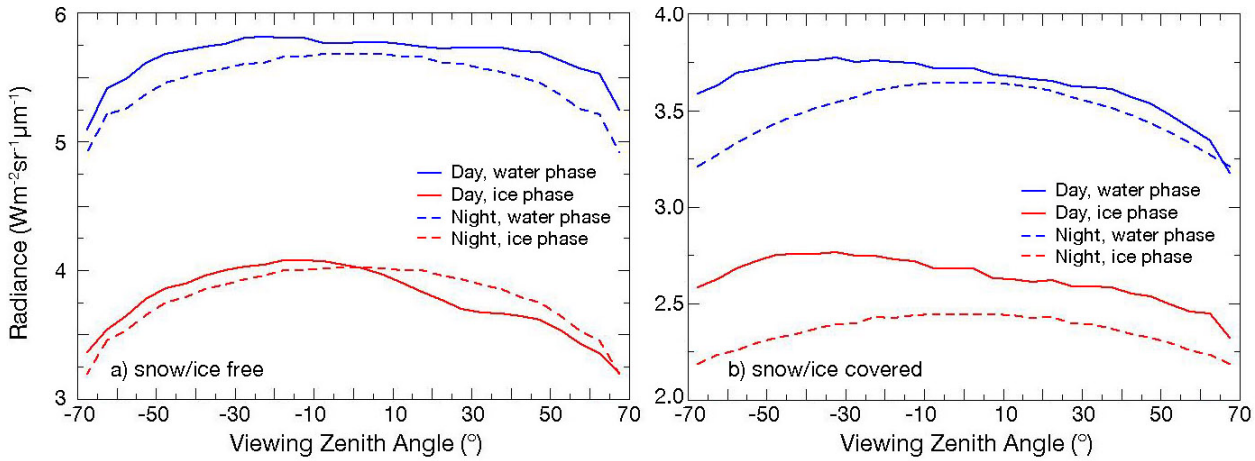

Fig. S5. Global average 8.55-μm radiance as a function of viewing zenith angle for JAJO 2019.

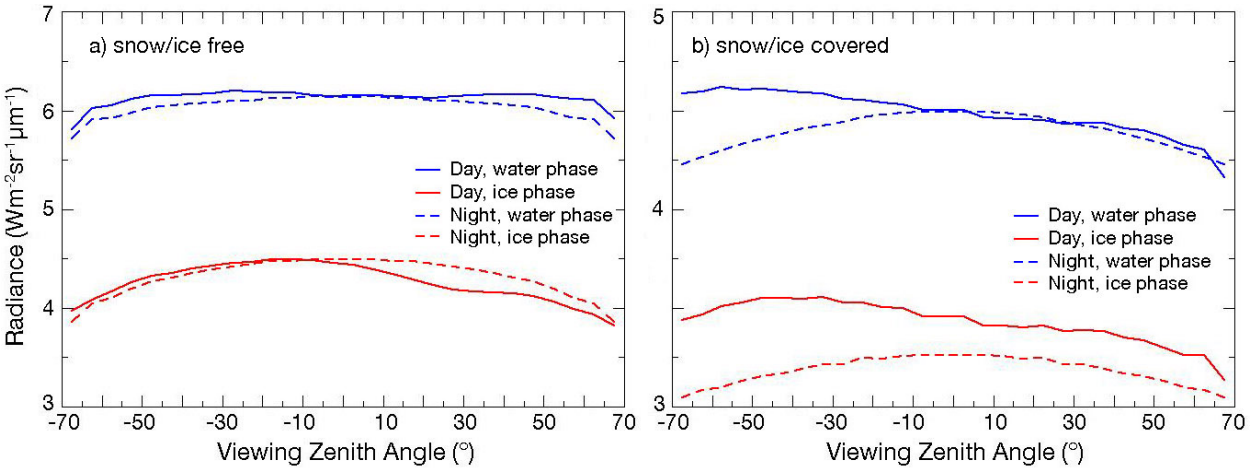

Fig. S6. Global average 11.9-μm radiance as a function of viewing zenith angle for JAJO 2019.

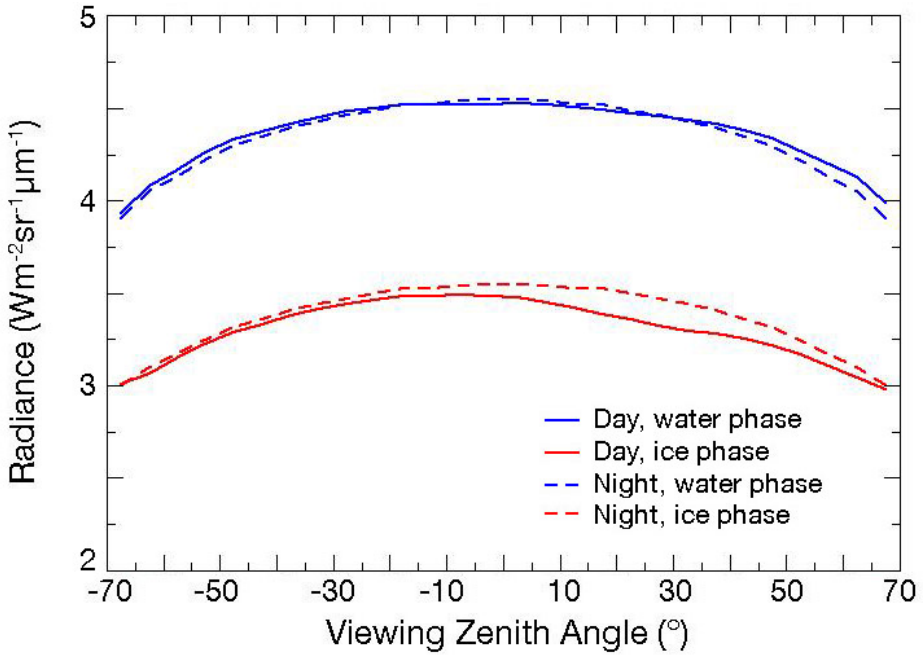

Fig. S7. Global average 13.3-μm radiance as a function of viewing zenith angle for JAJO 2019 over snow/ice free surfaces.

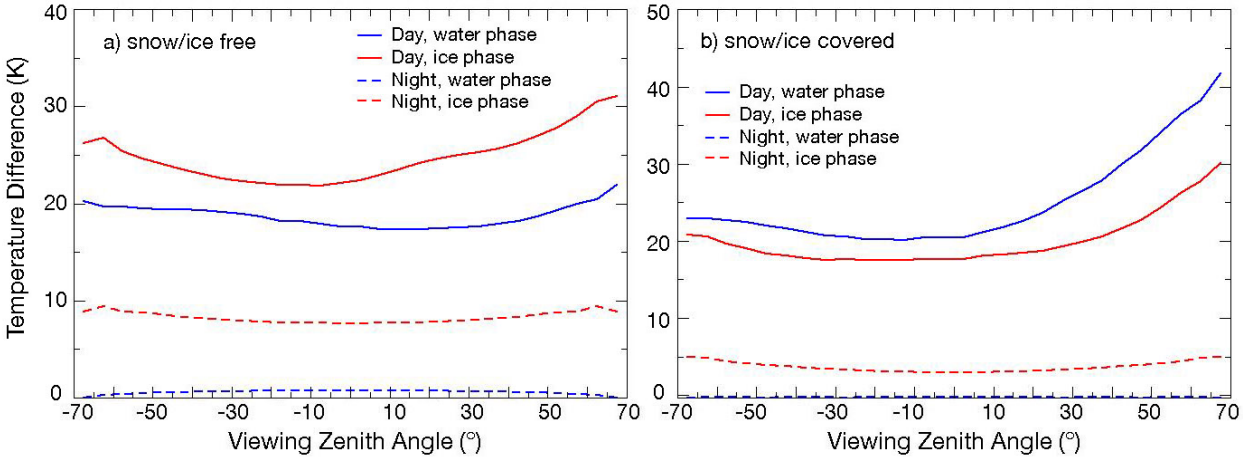

Fig. S8. Global average brightness temperature difference between 3.75-µm and 10.8-µm channels as a function of viewing zenith angle for JAJO 2019.

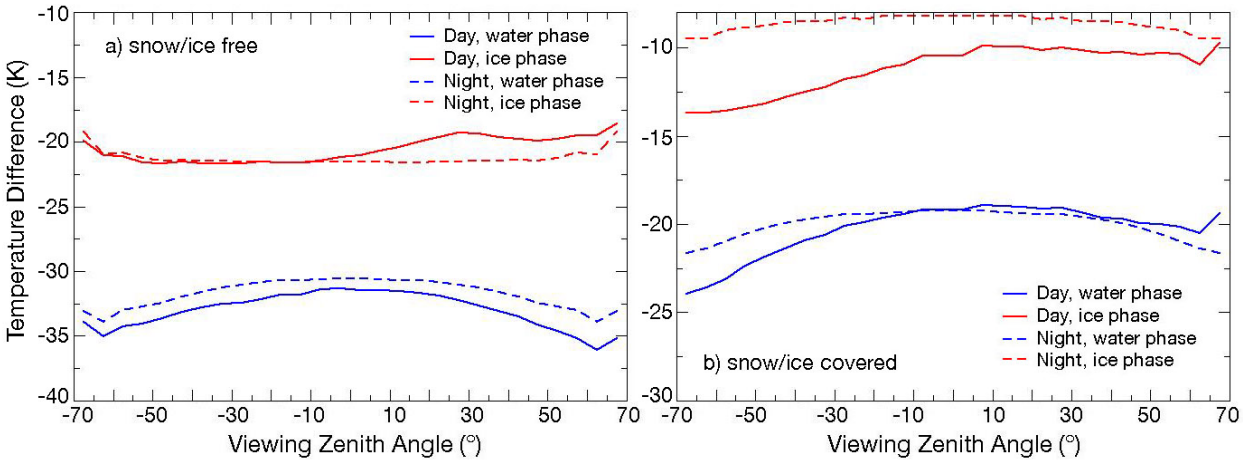

Fig. S9. Global average brightness temperature difference between 6.70-µm and 10.8-µm channels as a function of viewing zenith angle for JAJO 2019.

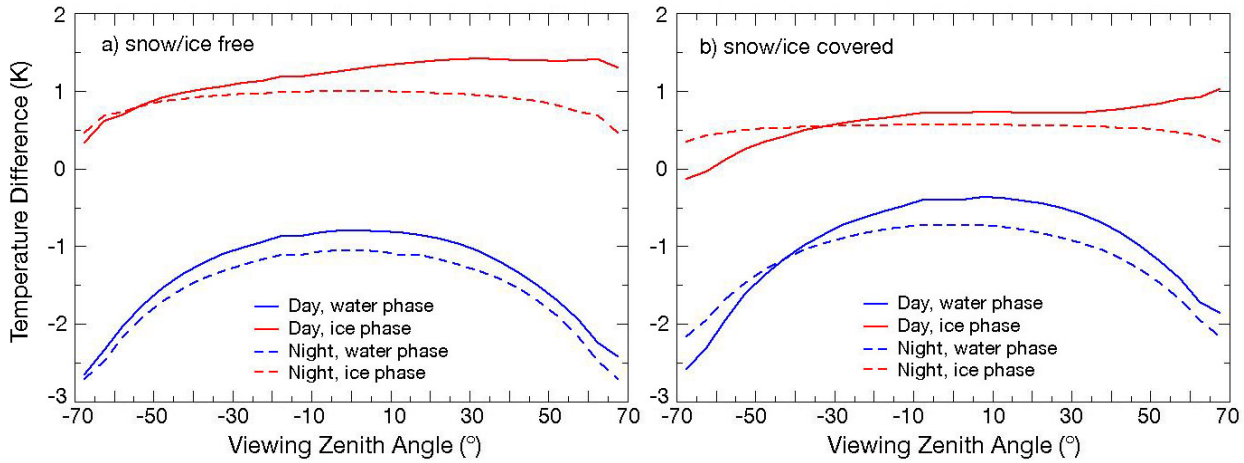

Fig. S10. Global average brightness temperature difference between 8.55-µm and 10.8-µm channels as a function of viewing zenith angle for JAJO 2019.

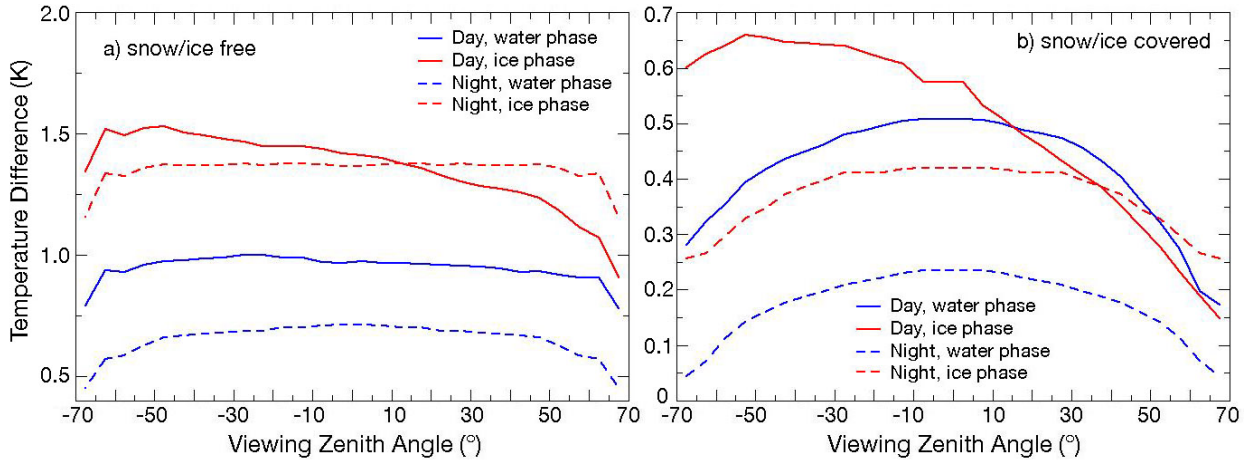

Fig. S11. Global average brightness temperature difference between 10.8-µm and 11.9-µm channels as a function of viewing zenith angle for JAJO 2019.

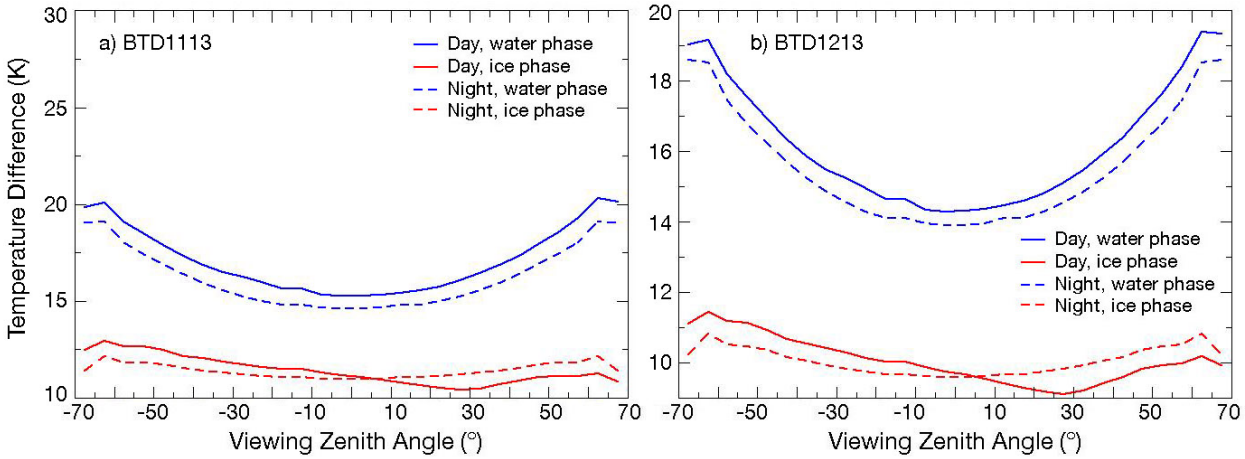

Fig. S12. Global average brightness temperature difference between (a) 10.8-µm and 13.3-µm and (b) 11.9-µm and 13.3-µm channels as a function of viewing zenith angle for JAJO 2019.

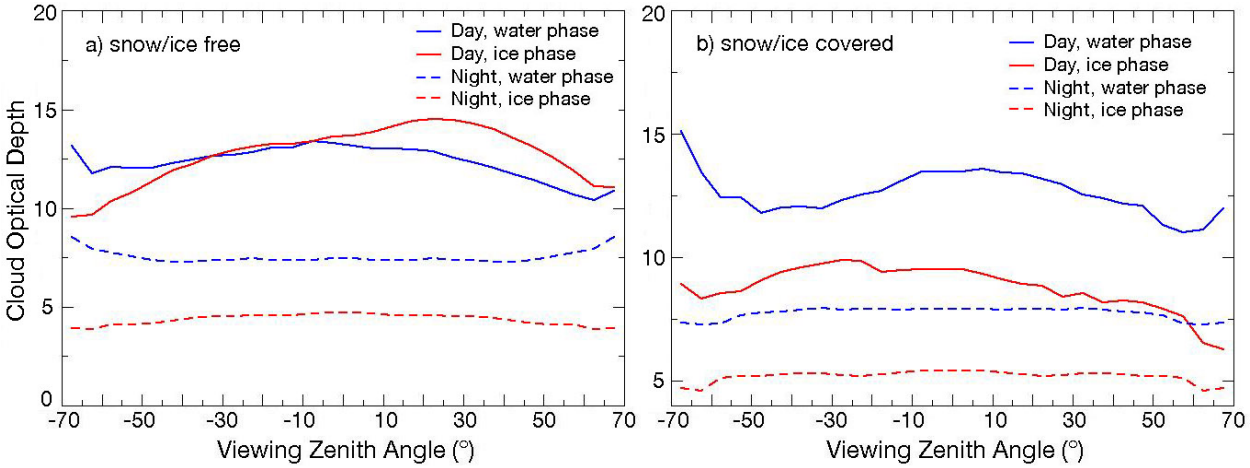

Fig. S13. Global average cloud optical depth as a function of viewing zenith angle for JAJO 2019.

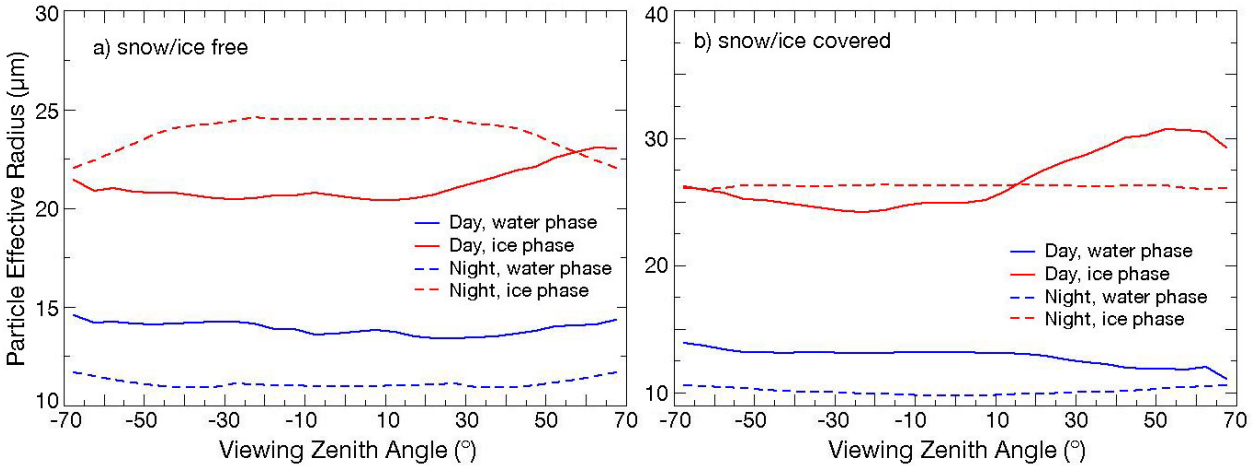

Fig. S14. Global average cloud particle effective radius as a function of viewing zenith angle for JAJO 2019.

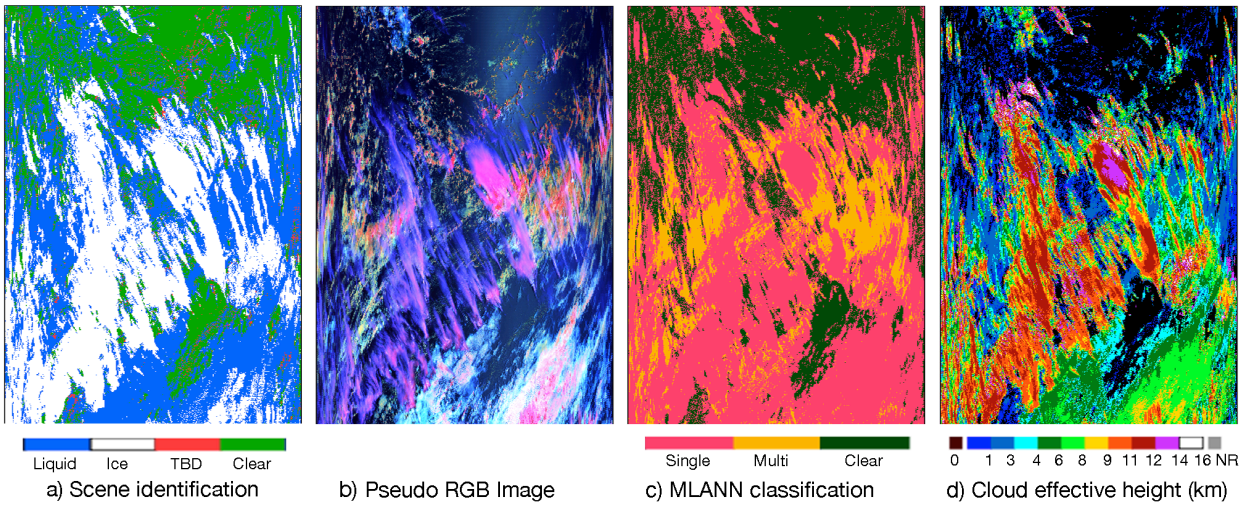

Figure S15. Cloud parameters derived from Aqua MODIS data between 1°N (top) and 13°N (bottom) around 135°W, at ~22:35 UTC, 16 April 2019. (a) CM4 pixel scene classification, (b) Pseudocolor RGB image, red: 0.64 μm reflectance, green: BT_{37}, green; blue: reverse BT_{11}. (c) MLANN classification, and (d) CM4 cloud effective height.

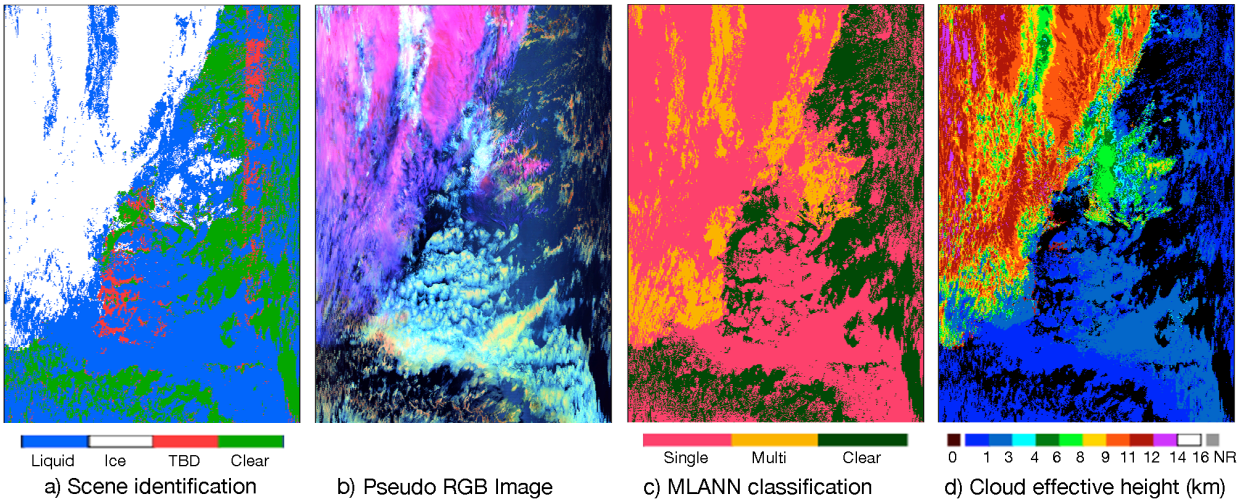

Figure S16. Cloud parameters derived from Aqua MODIS data between 29°N (top) and 17°N (bottom) around 140°W, at ~22:45 UTC, 16 January 2019. (a) CM4 pixel scene classification, (b) Pseudocolor RGB image, red: 0.64 μm reflectance, green: BT_{37}, green; blue: reverse BT_{11}. (c) MLANN classification, and (d) CM4 cloud effective height.

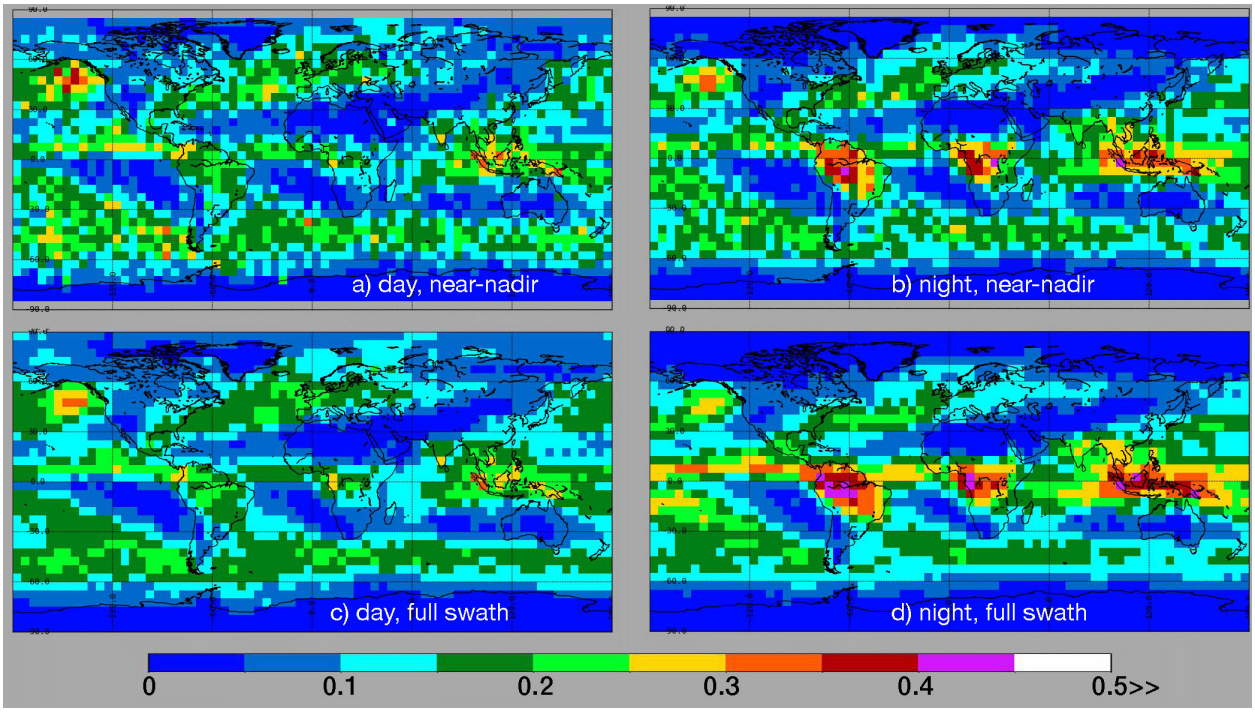

Fig. S17. Multilayer fraction of total cloud cover for JAJO 2013 using Aqua MODIS MLANN retrievals (top) at near-nadir (-18° < VZA , 3°), and (bottom) for all VZAs. Daytime on left, nighttime on right.